Available online at www.sciencedirect.com
ScienceDirect
Remote Sensing of Environment 107 (2007) 264–275
Remote Sensing of Environment
www.elsevier.com/locate/rse

Classification of glacier zones in western Greenland using albedo and surface roughness from the Multi-angle Imaging SpectroRadiometer (MISR)

Anne W. Nolin [a,*], Meredith C. Payne [b]

[a] Department of Geosciences, Oregon State University, Corvallis, Oregon 97331, United States
[b] College of Oceanic and Atmospheric Sciences, Oregon State University, United States

Received 18 March 2006; received in revised form 6 November 2006; accepted 6 November 2006

Abstract

The Greenland ice sheet has been the subject of mass balance and melt measurements over the past two decades and its margins have shown significant thinning in recent years. Surface characteristics of the ice sheet margins are strongly modified by the annual process of snow accumulation and melt. In this work, we explore spatial and temporal relationships between near-infrared albedo and surface roughness from the Multi-angle Imaging SpectroRadiometer (MISR) aboard NASA's Terra satellite. Our study area is a region in western Greenland in the vicinity of Jakobshavn Glacier and its upland drainage basin. We compute near-infrared albedo from MISR data using imagery over the April to September period for 2000 through 2005. Near-infrared albedo is inversely related to both snow age and melt intensity. We map surface roughness using the Normalized Difference Angular Index (NDAI) applied to MISR atmospherically corrected surface hemispherical-directional reflectance. In previous work, the NDAI has been correlated with surface roughness on the scale of about 70 m. We have further substantiated that relationship here. The NDAI and albedo images for each of the six years are used in an ISODATA unsupervised classification. Classification results for the individual years show year-to-year differences, which appear to depend on the number and temporal distribution of images with minimal cloud cover as well as interannual differences in ice sheet surface properties. The year 2003, which had the greatest number of images with minimal cloud cover, shows good correspondence with previously mapped glacier zones. However, we do not have an ISODATA class that corresponds to the dry-snow zone and we see greater differentiation between zones at lower elevations. Within each ISODATA class, distinct relationships between near-infrared albedo and surface roughness emerge and in all cases but one there is an inverse temporal relationship between albedo and roughness. The one class that shows a direct relationship between albedo and surface roughness is hypothesized to be the superimposed-ice zone. While still somewhat preliminary, these results suggest that concurrent measurements of near-infrared albedo and surface roughness have significant potential for ice sheet surface characterization as well as for ongoing monitoring.

Keywords: Albedo; Surface Roughness; Glacier zones; Greenland ice sheet; Jakobshavn Glacier

1. Introduction

1.1. Changes on the Greenland ice sheet

Ice and snow are showing a dramatic response to global warming and continued changes in polar ice have the potential to profoundly affect the Earth's climate even further (Abdalati & Steffen, 2001; Comiso, 2002; IPCC, 2001; Serreze et al., 2000; Vaughn & Doake, 1996). Feedbacks between albedo and temperature make it critical that we understand the extent and magnitude of albedo variations on polar ice sheets and the effects that melting and ablation have on surface energy balance (Knap & Oerlemans, 1996; Nolin & Stroeve, 1997; Steffen et al., 1993; Stroeve et al., 1997). On the Greenland ice sheet, results from Abdalati and Steffen (2001) indicate a linear increase in melt area of about 0.7% per year over the period from 1979–1999.

Although the high elevation interior of the Greenland ice sheet has been gaining mass over the 1992–2002 period (Zwally et al., 2005), the ice sheet margins have shown rapid thinning in the lower reaches of many outlet glaciers (Krabill et al., 1999, 2000;

* Corresponding author. Tel.: +1 541 737 8051; fax: +1 541 737 1200.
E-mail address: nolina@science.oregonstate.edu (A.W. Nolin).

0034-4257/$ - see front matter © 2006 Elsevier Inc. All rights reserved.
doi:10.1016/j.rse.2006.11.004

Paterson & Reeh, 2001; Thomas et al., 2000; Zwally et al., 2005). Coastal temperatures and ice sheet melt area have increased significantly (Abdalati & Steffen, 2001) but the thinning of outlet glaciers cannot be explained as ablation driven by surface energy balance. Important changes in outlet glacier ice dynamics are increasing glacier velocities and downstream thinning. Zwally et al. (2002) hypothesized that the thinning and acceleration of Jakobshavn Isbrae resulted from meltwater transmission from the surface to the glacier base thereby lubricating the glacier bed. Thomas (2004) attributed the rapid thinning of Jakobshavn Isbrae to breakup of the floating glacier tongue and some of the locally grounded ice. He developed equations demonstrating how this would reduce the backforce on the upper glacier allowing it to speed up and thin. Thomas also computed the effect of basal lubrication on backforce reduction. Rignot and Kanagaratnam (2006) have shown that not only are multiple glaciers in Greenland showing large increases in velocity and transport of ice to the ocean, but that this trend is occurring further north and is involving a greater number of glaciers than just a decade ago. These recent studies show the importance of ice dynamics to ice sheet mass balance and may be linked to changes in surface energy balance.

1.2. Albedo

Following definitions provided in Hapke (1993), a radiation incident on a surface that has both direct solar component and diffuse skylight components is termed "hemispherical irradiance". When the diffusely reflected radiation is measured the full upward hemisphere, this quantity is termed the bi-hemispherical albedo because both the illumination and measurement are hemispherical in nature. In contrast, reflectance measured at the top of the atmosphere by a satellite is termed the "bi-directional reflectance" because the illumination is composed of only direct beam solar radiation and the measurement is made with a narrow field of view and is also considered directional. At the surface, an atmospherically corrected measurement of reflectance is termed the hemispherical-directional reflectance because the illumination is hemispherical in nature (direct+diffuse irradiance) while the viewing geometry is again directional. "Narrowband albedo" is the spectral bi-hemispherical reflectance integrated over the spectral range of a single channel of a remote sensing instrument. In this investigation, "near-infrared albedo" refers to the narrowband albedo from near-infrared channel of the MISR instrument.

The dominant source of energy for ablation of ice sheets during summer comes from the absorption of solar radiation (e.g. Ambach, 1963; Braithwaite & Olesen, 1993). The degree of thermal forcing is controlled by ice sheet surface albedo, which is the ratio of reflected to incident solar radiation. Optical remote sensing measures reflected solar radiation and, unlike derived parameters from other types of remote sensing, provides a direct means for mapping glacier albedo (Knap & Oerlemans, 1996; Knap et al., 1999; Greuell & Knap, 2000; Greuell & de Ruyter de Wildt, 1999). Monitoring trends in ice sheet surface properties, especially surface albedo, is crucial to predicting rates of ice sheet melting and potential changes in the flow dynamics of outlet glaciers.

1.3. Surface roughness

Here, we define surface roughness (ξ) as the root mean squared deviation of the surface from a best fitting plane (Eq. (1)).

$$\xi = \sqrt{\frac{1}{n}\sum_{i=1}^{n}\left(z_{fi}-z_i\right)^2} \quad (1)$$

where, the z_{fi} are the heights of the fitted surface at n specified points and the z_i are the heights above that fitted surface.

Ice sheets exhibit a variety of surface roughness patterns, which can provide detailed information about the climatic and dynamic processes acting on the ice and snow (Herzfeld et al., 1999. Roughness is not only an indicator of surface–atmosphere interactions; the roughness scale also controls the degree of turbulent exchange between surface and atmosphere thereby influencing surface energy balance. In regions where the snow surface does not melt, eolian processes create features such as sastrugi (decimeter-scale erosional snow ridges) and snow dunes (meter-scale deposits). Warren et al. (1998) documented the effects of sastrugi on reflectance anisotropy, showing that oriented surface roughness on the Antarctic ice sheet significantly modifies the angular pattern of reflected radiation. The process of surface melt also leads to an increase in roughness as the smooth, dry snow gives way to melt features such as suncups, melt ponds, and supra-glacial channels. Extensive systems of crevasses mark the most dynamic portions of outlet glaciers and appear as the roughest parts of the ice sheet.

1.4. Research objectives

Albedo in the near-infrared portion of the spectrum (0.7–2.5 μm) is sensitive to diagenetic changes in surface snow properties, primarily snow grain size such as that induced by warming and surface melt (Nolin & Dozier, 1993; Warren, 1982). Moreover, the work of Nolin et al. (2002) points to the potential for, and innovative use of, multi-angle data for mapping surface roughness at subpixel resolution. The combination of near-infrared albedo and surface roughness has strong potential for improving our abilities to characterize ice sheet surface properties and their seasonal variability. The specific objectives of this study were to a) map and classify seasonal variations in NIR albedo and surface roughness over a range of ice sheet glacier zones; and b) examine the classification results in the context of previously mapped distributions of glacier zones.

2. Background and previous work

2.1. Greenland ice sheet mass balance and glacier zones

The term mass balance describes the relationship between accumulation and ablation of glacier ice. Accumulation occurs in the form of snow and ablation occurs through a combination of melting (both surface and basal melt), evaporation and sublimation, and iceberg calving. A negative mass balance means that a glacier is decreasing in total mass. For ice sheets such as Greenland, it is important to determine changes in mass

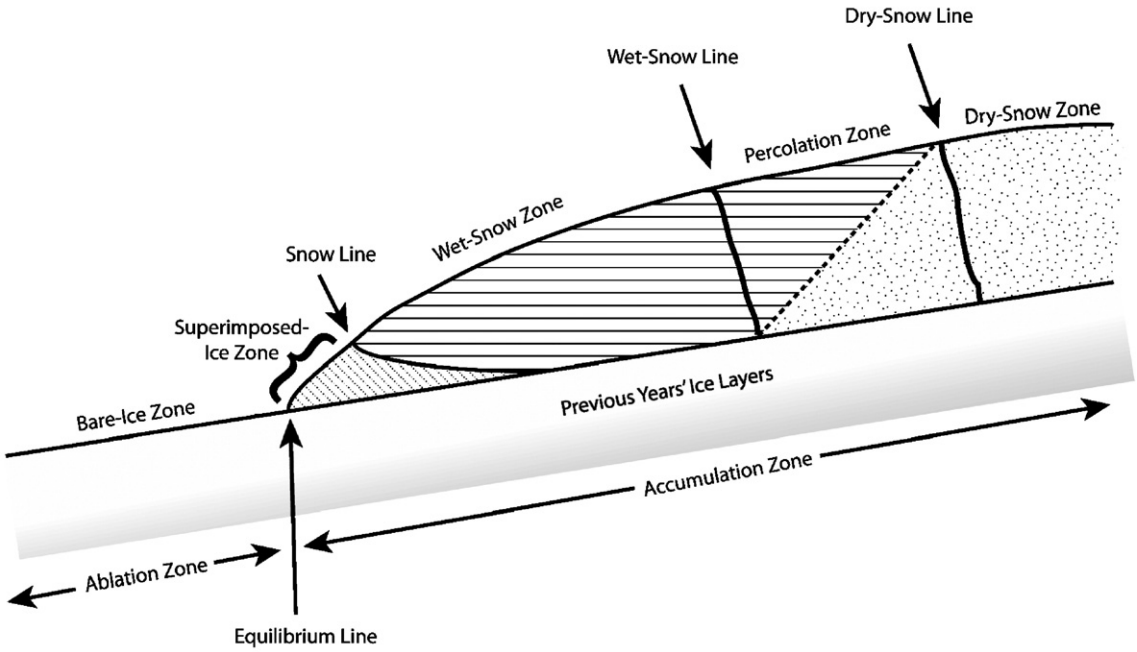

Fig. 1. Glacier zones on the Greenland ice sheet (after Benson, 1962; Paterson, 1994).

balance since a negative mass balance of a very large ice sheet will have major implications for sea level rise, freshwater fluxes into the ocean, and climate feedbacks.

With elevations ranging up to 3200 m, the Greenland ice sheet spans a wide range of snow and ice zones, which were measured and described by Benson (1962). Here, we follow the nomenclature of Paterson (1994), which is essentially the same as Benson with the exception of using the term "zone" rather than "facies". The dry-snow zone (Fig. 1), where there is no surface melt, is located at the highest elevations of the ice sheet. The percolation zone, where some melt occurs but meltwater percolates into the snowpack and refreezes, is next below the dry-snow zone in elevation. It is not easily distinguished from the wet-snow zone, where the complete annual accumulation of snow may experience meltwater percolation and refreezing. However, at the lower elevations of the wet-snow zone numerous melt ponds form and there are large areas of slush. Lower still is the superimposed-ice zone, where meltwater has refrozen onto the colder glacier ice surface. Because superimposed ice is created by melting and refreezing of the current year's snow, this zone is still considered part of the ice sheet accumulation area. The lowest elevation zone is the bare-ice zone, which represents the ablation region. In this region, each year's accumulation of snow and ice is fully melted and ice from previous years can be removed. The equilibrium line is defined as the boundary between the regions of net accumulation and net ablation, i.e. the lower boundary of the superimposed ice zone. The snow (or firn) line is the lowermost elevation where, at the end of the ablation season, snow (or firn) remains on the glacier surface, i.e. the upper boundary of the superimposed ice zone. Firn is densified snow that survives at least one melt season.

Early maps of Greenland ice sheet accumulation and ablation zones are based on limited in situ measurements (Bader, 1961; Benson, 1962; Mock, 1967). Optical remote sensing offers the ability to examine surface properties related to accumulation and ablation and to use the seasonal variability of surface properties to hone the delineations between glacier zones.

Satellite remote sensing to delineate glacier zones was first proposed by Østrem (1975) and has since been accomplished with mixed success using optical sensors (Bindschadler et al., 2001; Greuell & Knap, 2000; Hall et al., 1987; Williams et al., 1991), passive microwave sensors (Abdalati & Steffen, 2001; Mote & Anderson, 1995) and synthetic aperture radar (Echelmeyer et al., 1992; Fahnestock et al., 1993; Long & Drinkwater, 1994; Hall et al., 1995; Partington, 1998; Rott & Matzler, 1987). Optical sensors, which measure reflected light in the visible and near-infrared wavelengths, map surface variability on the ice sheets. In these wavelengths, it is possible to detect the snow line (as shown on Fig. 1), slush line (defined in Greuell & Knap, 2000 as the boundary that separates slush from snow that is wet but not completely saturated), and to a limited extent, the dry-snow zone and ablation area (König et al., 2001). To be reliable, such measurements must be made at the end of the ablation season. However, cloud cover can inhibit such measurements. Hall et al. (1987) use the term "reflectance zones" to describe the delineations that optical sensors can detect on glaciers. In that same vein, "radar zones" has also been suggested by Forster et al. (1996) to describe zonal variations on glaciers that can be detected by radar instruments. Active microwave (radar) pulses penetrate dry snow and backscatter is sensitive to surface and subsurface (meter-scale) ice sheet properties. For snow with high liquid water content the surface contribution dominates backscatter intensity. L- and C-band radar can detect the glacier ice zone, the firn line, the percolation zone, the wet-snow zone, and the dry-snow zone. Long and Drinkwater (1994) used multiple images from the Seasat-A

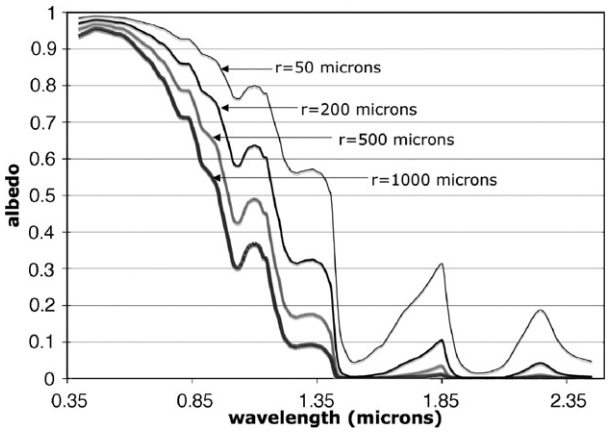

Fig. 2. The modeled spectral albedo of snow for a range of grain size radii. Values were computed using a two stream radiative transfer model (after Nolin & Stroeve, 1997).

Scatterometer over a single summer season to map glacier zones on the Greenland ice sheet and were successful at delineating the dry-snow, percolation, wet-snow and bare-ice zones. Passive microwave instruments can only detect broad changes; primarily the differences between regions of surface melt and dry snow. Several research groups have attempted to map the superimposed-ice zone from satellite but with limited success. Knap and Oerlemans (1996) used data from the Advanced Very High Resolution Radiometer (AVHRR) to map the surface albedo of the Jakobshavn drainage basin. They conjectured that a darker region immediately below what appeared to be the snow line was a region of superimposed ice. While the position of this ice facies is correct in relation to snow and exposed glacier ice, the conclusion was preliminary and did not lead to an automated means of detecting superimposed ice from remote sensing data. In one instance, Marshall et al. (1995) were able to distinguish between superimposed ice and bare glacier ice on the basis of surface roughness differences detectable in synthetic aperture radar (SAR) data. Furthermore, Engeset et al (2002) found that SAR showed some potential for mapping superimposed ice on a glacier in Svalbard. König et al. (2002) had mixed success using SAR to map superimposed ice on two glaciers in Svalbard. They attributed differences in radar backscatter to varying air bubble content and surface roughness.

2.2. Snow grain size, surface energy balance and albedo

It is well established that the albedo of clean snow is controlled primarily by the grain radius of the surface layer of snow and that the relationship between albedo and grain size is especially sensitive in the near-infrared wavelengths (Choudhury, 1981; Dozier et al., 1981; Hyvärinen & Lammasniemi, 1987; Nolin & Dozier, 1993, 2000; Wiscombe & Warren, 1980; Warren, 1982; Warren & Wiscombe, 1980). Grain growth in dry snow occurs with snowpack aging (Colbeck, 1982, 1983) and proceeds rapidly as grain clusters form in wet snow (Colbeck, 1979, 1982). In their study of the Greenland ice sheet, Nolin and Stroeve (1997) used an energy balance model to show how changes in snowpack energy balance modify the surface grain size and thereby affect albedo. They were able to accurately relate the increase in grain size with positive snowpack energy balance and could detect the onset of melt by the decrease in albedo that corresponded with rapid grain growth in wet snow. Fig. 2 shows the modeled spectral albedo for snow of differing grain radii, representing the transition from new snow (50 μm grain radius) to aging and melting snow (200 and 500 μm grain radii) to saturated snow with grain clusters (1000 μm grain radii).

2.3. Multi-angle remote sensing of ice sheet albedo and surface roughness

Multi-angle views can provide unique information about the ice sheet surface, at scales below that of the nominal spatial resolution, that can be used to improve our characterization of climate and ice dynamics processes. The Multi-angle Imaging SpectroRadiometer (MISR) instrument on the Terra satellite platform provides near-concurrent multiple views of a surface at several viewing geometries, with a spatial resolution of 275 m (Diner et al., 2002; Table 1). It has excellent radiometric resolution, so variations in surface roughness or reflectance may be quantified precisely.

It has also been shown that MISR data can be used as a proxy for surface roughness. Nolin et al., 2002 developed a normalized difference angular index (NDAI) using a combination of forward and backward scattered radiation.

$$\mathrm{NDAI} = \frac{\rho_{-60} - \rho_{+60}}{\rho_{-60} + \rho_{+60}} \quad (2)$$

where, ρ_{-60} and, ρ_{+60} are the bi-directional reflectance (for top-of-atmosphere) or hemispherical-directional reflectance (for surface quantities) in the MISR red channel, from MISR's 60° aft and forward viewing cameras, respectively. For a descending orbit in the Arctic, the forward viewing camera is seeing forward scattering and the aft camera is seeing backward scattering because the sun is to the south. Forward scattering is associated with generally smooth surfaces while backward scattering dominates when a surface is rough. Thus, a positive (negative) NDAI value indicates that backward (forward) scattering exceeds forward (backward) scattering and that the surface is rough (smooth). The NDAI was shown to be correlated with surface roughness derived from an airborne laser altimeter (Nolin et al., 2002). However, in that initial comparison, the lidar and MISR data were from different years. Following the definition of surface roughness

Table 1
Description of the MISR instrument

Camera angles	±70.5°,±60.0°, ±45.6°,±26.1°, 0°
Spectral bands	448 nm (blue), 558 nm (green) 672 nm (red), 866 nm (near IR)
Pixel size	275×275 m (all bands in nadir camera and red bands in all other cameras) 1.1×1.1 km (blue, green, and near IR bands in fore and aft cameras)
Swath width	380 km
Quantization	14 bits, square-root encoded to 12 bits

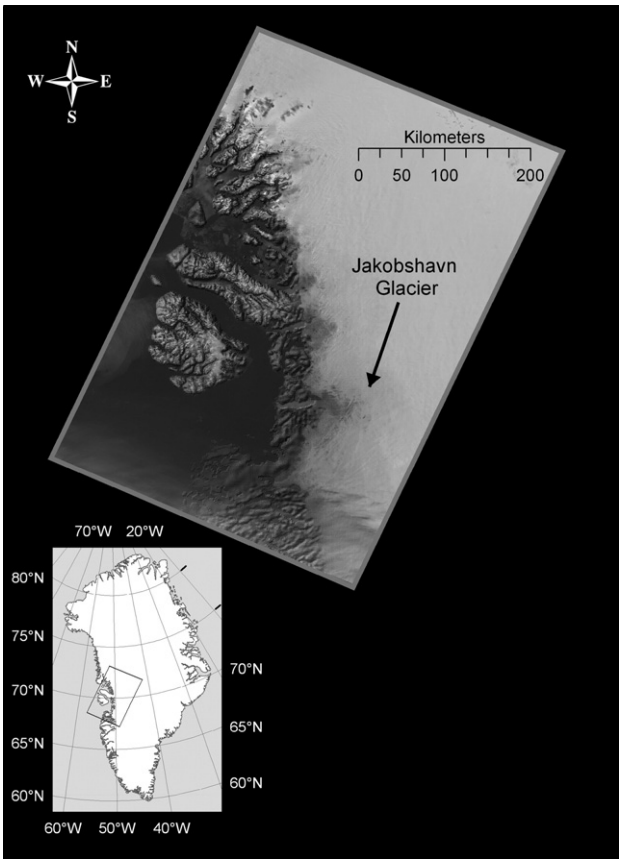

Fig. 3. Locator map of the study area. The upper inset is a near-infrared albedo image from 30 May 2002 that has been draped over a hillshade relief image derived from a digital elevation model.

in Eq. (1), hereafter we refer to NDAI roughness as NDAI and lidar roughness as ξ_{lidar}.

3. Methodology

Our study area is the Jakobshavn Glacier and its upland drainage basin (Fig. 3), spanning the full range of ice sheet zones. We compute NDAI and near-infrared narrowband albedo (hereafter referred to as "NIR albedo") for the area and examine the temporal patterns of these two quantities over the course of six summers (2000–2005). We use the NDAI and NIR albedo images as input to an unsupervised classification. These are described in greater detail below.

3.1. Description of the study area

The Jakobshavn Glacier in west Greenland (Fig. 3) is one of the fastest flowing glaciers in the world, with 12 km per year movement (Joughin et al., 2004). Elevations in the study area range up to 2800 m and the area comprises potentially all of the Benson glacier zones including the bare-ice zone, superimposed-ice zone, wet-snow zone, and percolation zone (and possibly the lower portion of the dry-snow zone). In the nomenclature used for ordering MISR data, the study area consists of MISR Paths 9–10, Blocks 32–35.

3.2. Computing near-infrared albedo from MISR

To compute NIR albedo, we started with MISR Level 1B2T terrain-projected top-of-atmosphere scaled radiance data. Image dates and orbit numbers are listed in Table 2 and span six summers (2000–2005). Images were examined individually to ensure that only those with minimal cloud cover (<20%) were used in the analysis. Following the method of Nolin and Stroeve (1997), each image was georeferenced, converted from top-of-atmosphere scaled radiance to top-of-atmosphere reflectance, atmospherically corrected using the 6S atmospheric radiative transfer model (Vermote et al., 1997), and converted to NIR albedo.

3.3. Computing NDAI from MISR

As before, we started with MISR L1B2T terrain-projected top-of-atmosphere scaled radiance data. Each image was georeferenced, converted from top-of-atmosphere scaled radiance to top-of-atmosphere reflectance, and atmospherically corrected. Here, we used the surface hemispherical–directional reflectance data to compute NDAI (Eq. (2)). Unlike NIR albedo, the red channel values used to compute NDAI retain their viewing angle dependencies. Low values (negative) of NDAI correspond to smoother surface conditions and higher (positive) values correspond to rougher surface conditions. To further test the assumption that NDAI is a good proxy for surface roughness,

Table 2
List of MISR image acquisition dates and orbit numbers used in this study

2000		2001		2002		2003		2004		2005	
Orbit #	Date	Orbit #	Date	Orbit #	Date	Orbit #	Date	Orbit #	Date	Orbit #	Date
1606	6 Apr	6863	2 Apr	12557	28 Apr	17916	1 May	22809	1 Apr	28634	6 May
2771	25 Jun	7329	4 May	12921	23 May	18149	17 May	22940	10 Apr	28867	22 May
3368	5 Aug	7795	5 Jun	13023	30 May	18513	11 Jun	23042	17 Apr	28998	31 May
3703	28 Aug	7897	12 Jun	13154	8 Jun	18615	18 Jun	23406	12 May	29100	7 Jun
		8130	28 Jun	13489	1 Jul	18746	27 Jun	23508	19 May	29231	16 Jun
		8261	7 Jul	13955	2 Aug	18848	4 Jul	23741	4 Jun	29464	2 Jul
		8363	14 Jul	14421	3 Sep	18979	23 Jul	23974	20 Jun	29930	3 Aug
						19212	29 Jul			30498	11 Sep
						19314	5 Aug				
						19780	6 Sep				
						19911	15 Sep				

we compared these data with near-concurrent airborne lidar data using multiple transects over the Jakobshavn Glacier area. For this comparison (described in Section 4.1, below), we used the same methodology as described in Nolin et al. (2002).

3.4. ISODATA classification

The basis for the classification is the temporal changes in NIR albedo and NDAI over the course of the sunlit season. Images for each summer were arranged in temporal order and this multi-temporal sequence was then classified using an iterative self-organizing data analysis (ISODATA) unsupervised classification method (Duda & Hart, 1973). The ISODATA method is a well-known clustering technique that assigns pixels to a class based on class means. The number of classes is specified over a range and the classification determines the final number. Multiple iterations refine the class means and class boundaries as the algorithm minimizes the within-class variance and maximizes the between-class distance. Here, the maximum within-class difference was specified to be 1.0 standard deviation and the minimum distance between classes was specified to be 5.0 standard deviations. The minimum and maximum number of specified classes was 6 and

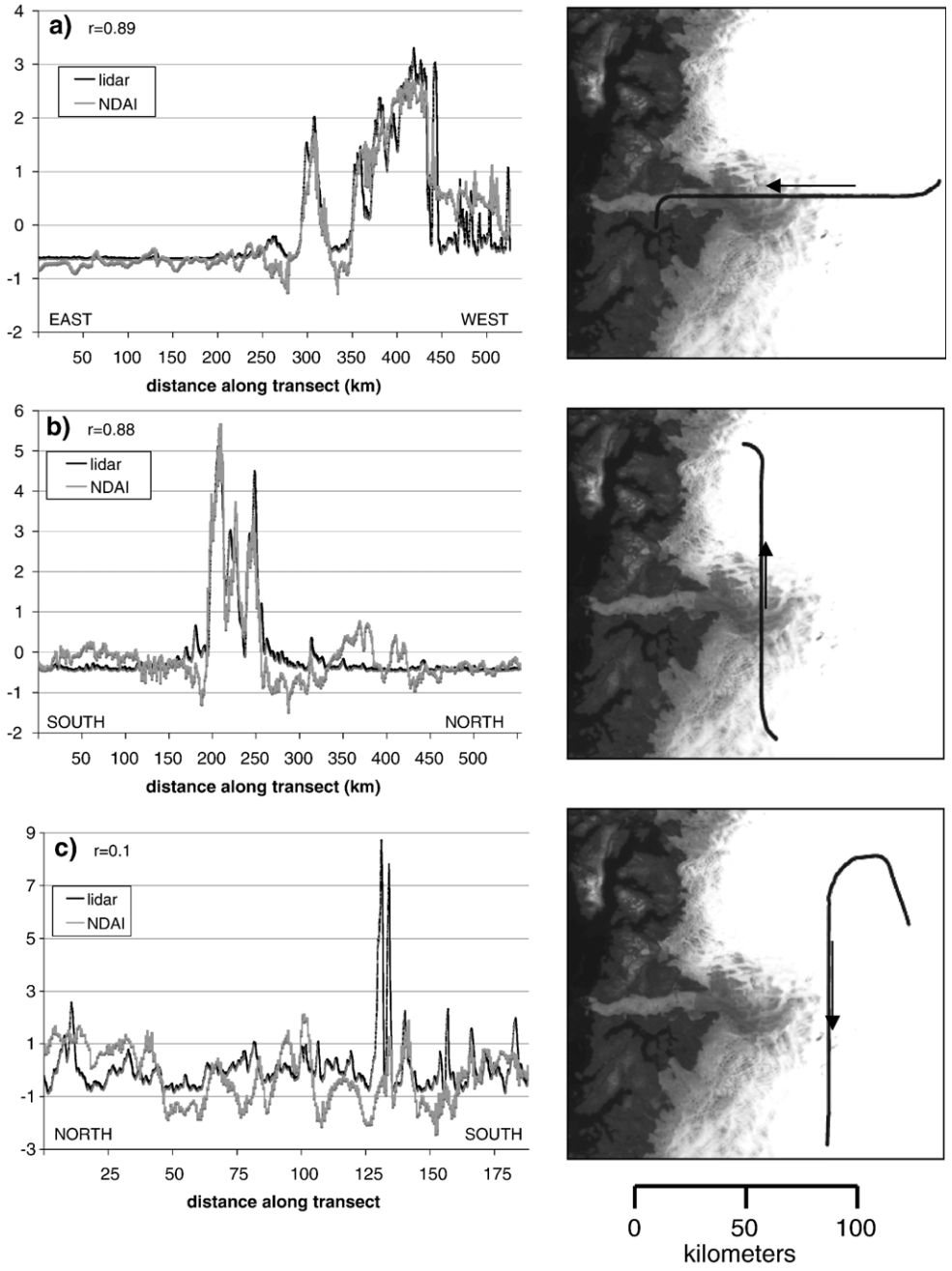

Fig. 4. Comparison of normalized NDAI and ξ_{lidar} for three transects. The arrow indicates the direction of travel of the airborne lidar. Panels (a) and (b) show very close agreement between the two measures of roughness, across the main portion of Jakobshavn Glacier. Panel (c) shows weak statistical correlation for a relatively smooth part of the ice sheet.

20 respectively. The classifier was run for 20 iterations with a class change threshold of 3%.

4. Results and discussion

4.1. Comparison of NDAI and ξ_{lidar}

Pre-computed airborne lidar-derived surface roughness data from May 30, 2002 (supplied by W. Krabill of the NASA/Wallops Flight Facility) were compared with NDAI values from May 31, 2002. Lidar tracks in which the corresponding MISR data showed clouds were eliminated. The lidar derives surface altitude by measuring the time of travel between aircraft and surface. The lidar surface roughness values were computed (following Eq. (1)) over a 70-m portion of the lidar transect.

Fig. 4 shows the comparisons for three tracks in the Jakobshavn Glacier area. For each track, both NDAI and ξ_{lidar} have been normalized by subtracting the mean and dividing by the standard deviation (as in Nolin et al., 2002). Thus, these comparisons are based on relative variations in roughness rather than absolute

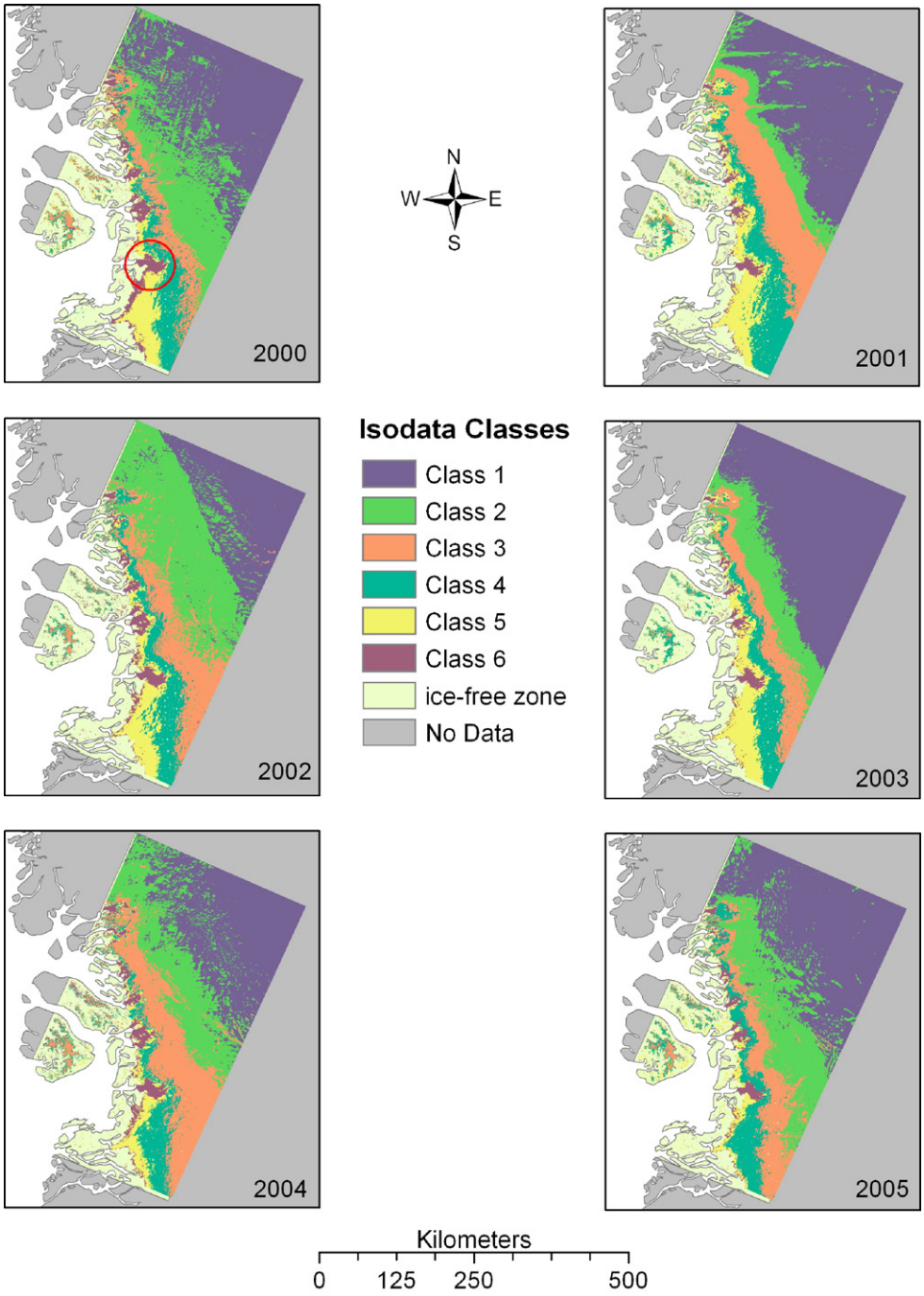

Fig. 5. ISODATA classification results for 2000–2005. The red circle shown on the results for 2000 indicates the fast-moving portion of the glacier.

roughness. The middle panel shows a north–south track that passed over the main portion of the glacier. The Pearson's correlation coefficient, r, is 0.88. The top panel also shows a strong correlation between NDAI and ξ_{lidar} ($r=0.89$) as it traverses the glacier from east to west. Although the two sets of normalized roughness values are not comparable in terms of absolute magnitude, the good correlations show that they get rough in the same portions of the transects. The bottom panel, from a track crossing a relatively smooth portion of the ice sheet located east of the previous tracks shows only a weak correlation. However, visual comparison shows congruence in certain portions of the track suggesting that NDAI still contains useful information. All three panels show that the agreement between NDAI and ξ_{lidar} is lower for smoother portions of the ice sheet. In these areas of the transect, NDAI demonstrates a higher degree of roughness and overall variability relative to its mean value than do the lidar data. This may result from a difference in the spatial scale of pre-processed ξ_{lidar} data (70-m) and the MISR spatial resolution (275-m). While the original lidar data accurately record elevation at 1-m intervals, the processing to derive lidar roughness is computed over 70-m fitted surfaces. Therefore, undulations that exceed 70 m will not be detected with lidar roughness data processed at this scale. Close visual examination of enlarged versions of the near-infrared albedo images (not shown) shows surface shading differences suggesting topographic variability at a scale that exceeds the 70-m lidar processing.

4.2. Analysis of classification results

Results of the ISODATA classification using annual time series of NIR albedo and NDAI reveal coherent spatial patterns that vary with elevation and position relative to the fast-moving portion of Jakobshavn Glacier. For each year, the clustering algorithm computed six classes of ice sheet surface types. Fig. 5 shows the classification results for all six years. There are year-

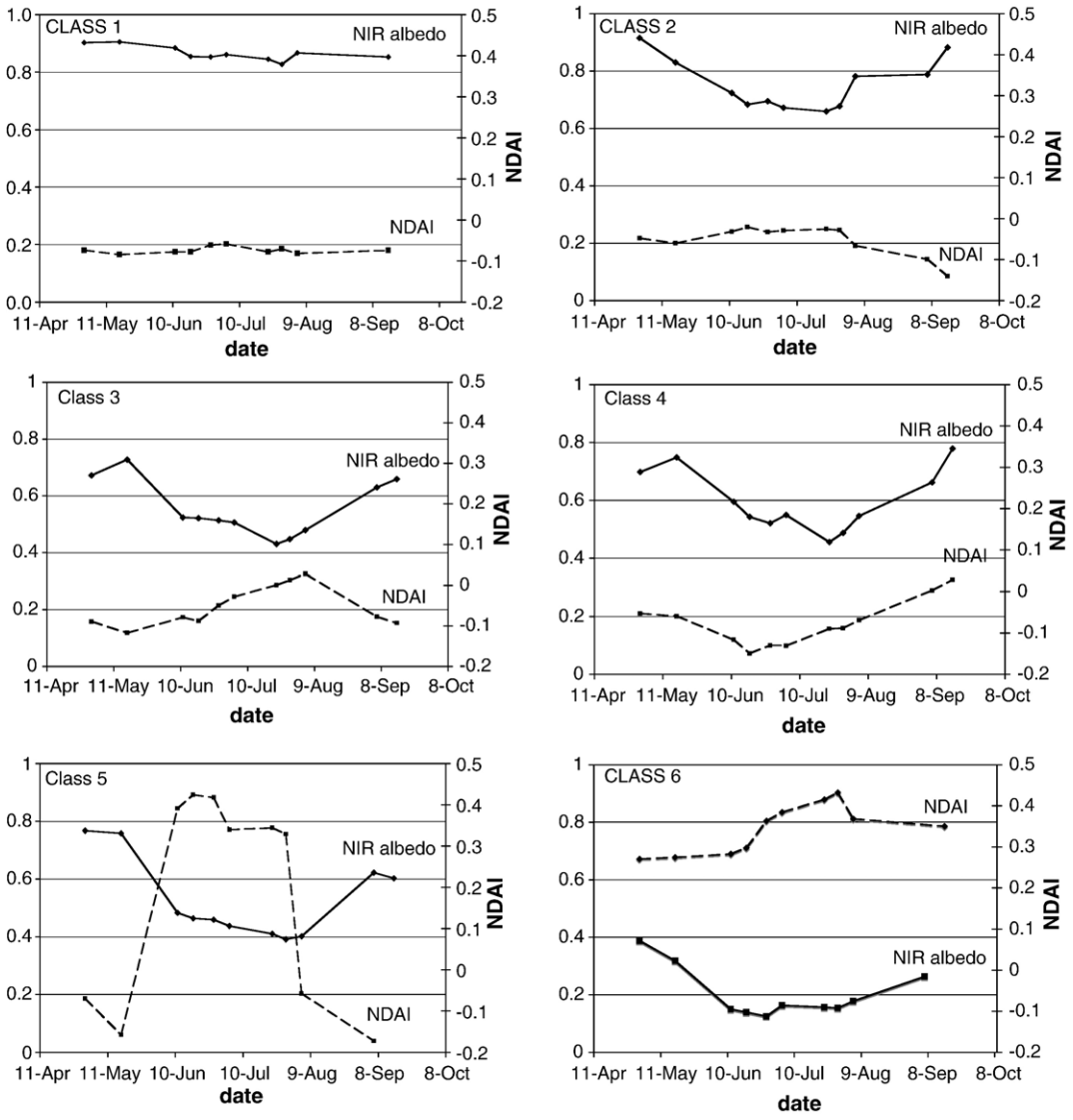

Fig. 6. Time series plots of NIR albedo (solid lines) and NDAI (dashed lines) from 2003 for areas that are representative of each class. Locations of the representative areas are shown on Fig. 7.

to-year differences in the geographic boundaries between the classes that can be explained by differences in a) the number of images with acceptably low (<20%) cloud amounts available in each year; b) the temporal distribution of the images within each year; and c) ice sheet surface properties. Table 2 gives the dates for each image. In 2000, there were only four relatively clear images, but their dates ranged from early April through late August. In 2001, there were seven acceptable images used but they only extended into mid-July. Although 2002 had the same number of images as 2001, acquisition dates ranged from April through September. The summer 2003 had by far the most images with 11 acceptable images whose dates ranged from early May to mid-September. 2004 was quite limited in range with acceptable images available only into late June. In 2005, we used eight images that ranged from April to early September. Given the temporal distributions of imagery, it is difficult to distinguish between classification differences due to data availability and those due to true interannual variability of ice sheet surface properties. Therefore, we focus our interpretation of results on 2003, which had a large number of acceptable images spanning the full melt season.

4.3. NIR albedo and NDAI differences between classes for 2003

Using data from 2003, a representative region was selected from each class and used to show the temporal changes in NIR albedo and NDAI (Fig. 6). Because of our *a priori* specification of within-class and between-class standard deviations (Section 3.3),

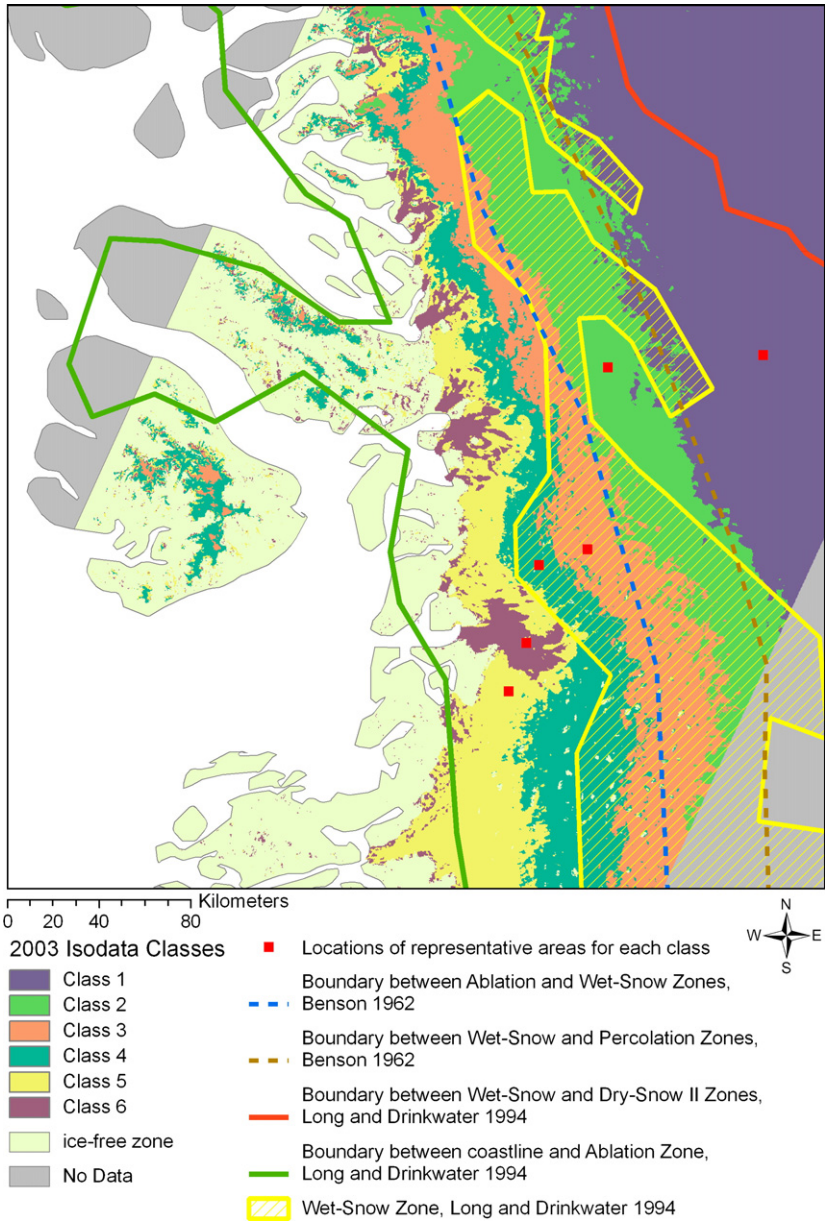

Fig. 7. MISR-derived ice sheet classes for 2003. Superimposed on the classification are the boundaries for glacier zones from Long and Drinkwater (1994) and Benson (1962) and the locations for the representative areas for each class that are used in Fig. 6.

we know that the between-class differences are five times greater than the within-class variability, assuring class uniformity and significant differences between classes. Each of the representative areas was selected by choosing a 10 × 10-pixel (7.56 km^2) square that was cloud-free for all dates of the time series and that was at least 20 pixels away from another class.

Class 1 has relatively low variability in both NIR albedo and NDAI. NIR albedo reaches a minimum of 0.83 in August followed by a late summer increase that was likely the result of new snowfall. Surface roughness in Class 1 as inferred from NDAI is consistently negative implying a smooth surface; there is only a small increase in NDAI in July and August. In Class 1, NDAI has a weakly inverse relationship with NIR albedo. The small decrease in albedo is consistent with a small amount of melt and the corresponding grain growth (Nolin & Stroeve, 1997).

Class 2 shows a more significant decrease in albedo during the summer, with a minimum albedo value of 0.66. It is unlikely to find an albedo value this low unless extensive melt is occurring (Nolin & Stroeve, 1997); sub-resolution melt ponds may also have formed. There is an inverse relationship between albedo and surface roughness; in summer roughness increases slightly more strongly than for Class 1.

Class 3 has a minimum albedo of 0.43 and has a large increase in NDAI in July–August. The area comprising Class 3 has numerous melt ponds (as seen in July and August images, not shown), which are likely responsible for the low albedo values in those months.

Class 4 has an albedo decrease similar to that of Class 3 (minimum of 0.45) but, unlike all the other classes, it shows a decrease in surface roughness in early summer. This will be discussed further in the next section. However, like Class 3, Class 4 also has numerous melt ponds in July–August (not shown).

Class 5 has still lower minimum albedo (0.39) with large decreases early in the melt season. NDAI shows a strong early summer increase going from slightly negative to strongly positive values indicating a high degree of surface roughness.

Class 6 represents the portion of study area with extensive crevasses. This class has a consistently low NIR albedo (minimum of 0.12) and high NDAI throughout the summer. Lastly, there is the portion of the study area that either did not have continuous snow or ice cover during the entire summer or was covered by rock debris and could not be distinguished from non-ice covered areas. This area was not classified and is labeled in Figs. 6 and 7 as the "ice-free zone".

It is useful to compare the geographic boundaries of our ISODATA classes with previously mapped glacier zones. In Fig. 7, we have overlain glacier zone boundaries from two previous studies: Long and Drinkwater (1994, henceforth LD) and Benson (1962). For consistency in terminology, we use the authors' terminology for their glacier zones. Locations of the representative areas selected for each class are shown in Fig. 7. Class 1 roughly corresponds with the lower boundary of LD's and Benson's Percolation zone. Benson (whose measurements were made in the 1950s) did not find a dry-snow zone in this region. From the ISODATA classification, we do not see any evidence of the LD's Dry Snow II zone. However, LD determined their Dry Snow II zone from radar data, which are related to different physical properties such as internal scattering, rather than temporal changes in surface roughness and albedo. It is likely that this radar-derived zone is not expressed as a surface property and therefore was not recognized by Benson, nor by our classification. The wet-snow zone of LD appears to encompass ISODATA Classes 2 and 3 as well as portions of Class 4. Benson's wet-snow zone also corresponds with Classes 2 and 3. The lower geographic boundary of LD's wet-snow zone tracks Class 4 reasonably well, especially in the southernmost part of the class. Class 6 maps the downstream (and most heavily crevassed) parts of the Jakobshavn and other glaciers in the region.

Of perhaps greatest interest is Class 4, which was the only ISODATA class that showed a decrease in NDAI during the summer. While LD indicate decreasing roughness for their entire wet-snow zone, our study shows decreasing roughness only for this relatively narrow class. Based on previous work by Marshall et al. (1995) showing that superimposed ice is smoother than glacier ice in the ablation zone, we hypothesize that Class 4 represents the superimposed-ice zone. Its location below the lower geographic boundary of the wet-snow zone of LD also fits with the conjecture of Knap and Oerlemans (1996) and mapping efforts of Greuell and Knap (2000) that this zone represents superimposed ice.

At first glance, it is surprising that the boundaries between the various glacier zones do not appear to have shifted substantially since the middle of the previous century especially given that melt on the ice sheet has significantly increased over the past decade (Abdalati & Steffen, 2001). Since our work (and that of Benson) indicates that the dry-snow zone is not within the study region, any shift in the boundary between the percolation and dry-snow zones will not be detected. Without the benefit of field validation, we speculate that although the boundaries between glacier zones may be have been fairly consistent for all but the dry-snow zone, there may have been other changes within the wet-snow and percolation zones that are climatologically important such as earlier melt onset and larger melt ponds. The overall melting area may have increased substantially (outside of our study area) but the extents of the wet-snow zone and bare-ice zones may not have changed much over time, only the timing and intensity of melt. This remains as a topic for future investigation.

4.4. Sources of error

A number of error sources need to be considered in the analysis and interpretation of the NIR albedo and NDAI data and the ensuing classification. First, the NIR albedo data are only accurate to within about 7% (Stroeve & Nolin, 2002) and subtle recorded shifts in albedo may not be significant. Secondly, the NDAI is not an absolute measure of surface roughness and, while it has been shown that there is a good correlation between NDAI and ξ_{lidar} at the 70-m scale, effects of solar and viewing geometries on the detectability and scales of roughness remain to be quantified. For instance, the orientation and scale of rough features relative to the illumination will likely influence NDAI. Furthermore, the scale of the lidar measured roughness and NDAI roughness estimates are not

always congruent over the smoother portions of the ice sheet where broad undulations affect the NDAI but are not seen in the airborne lidar measurements because the latter are processed to fit a 70-m planar surface to the elevation data. Ostensibly, if the airborne lidar data had been processed using a longer planar fitted surface, these undulations would have been detected.

The ability of the ISODATA classifier to produce separable classes is determined by the user-specified bounds on within- and between-class variability but it can also be limited by the input data. Year-to-year differences in the spatial extent of the classes depend on the number and temporal distribution of images acquired during the sunlit season and will influence the accuracy of the classification. Compared with 2003, summers in which there are few images or where they are not evenly distributed show more irregular and somewhat diffuse boundaries between classes (possibly the effects of clouds). Ideally, images acquired every 1–2 weeks would provide optimal sampling of changes in ice sheet surface properties. However, cloud cover and the frequency of coverage by the MISR instrument are limiting factors. Most importantly, without in situ data our understanding of the meaning of the classification results prevents us from drawing firm conclusions. However, it is clear that there are distinct regions of the ice sheet that behave in a spatially coherent fashion with regard to temporal patterns of NIR albedo and NDAI.

5. Conclusions

ISODATA classes derived from MISR NIR albedo and NDAI images show distinct spatial patterns that follow the patterns of previously mapped glacier zones. The exception is in the lack of a recognized dry-snow zone as had been previously mapped by Long and Drinkwater. A potentially important finding is that of a narrow, low elevation ISODATA class in which both NIR albedo and NDAI decrease over the course of the melt season. This is in distinct contrast to other classes where roughness increases with melt. We hypothesize that this class corresponds to the superimposed-ice zone because a) superimposed ice is smoother than bare glacier ice and firn and, b) it is in the proper position in relation to other glacier zones on the ice sheet. Conclusive evidence will require in situ measurements. However, these results point to the value of remote sensing to identify areas of unique ice sheet surface properties and to provide guidance for locating future field measurements.

MISR can be used to concurrently retrieve both albedo and NDAI at 275-m spatial resolution, providing a high degree of spatial detail. In addition to their potential for ice sheet surface characterization, albedo and surface roughness are also needed to improve surface energy balance models. Multi-angle observations are also needed to improve our understanding of patterns of bi-directional reflectance. Angular distribution models (ADMs) are used by instruments such as the Clouds and the Earth's Radiant Energy System (CERES), which monitors the Earth's radiation budget. To accurately measure changes in reflected energy, sub-grid variability in albedo, surface roughness, and surface reflectance anisotropy must be known. These measurements from MISR are an important first step in improving CERES ADMs over the ice sheet thereby leading to a more accurate Arctic energy budget. However, there is still the need for in situ validation, especially with regard to understanding the relationships between glacier zones and the albedo/roughness classes identified here. Furthermore, there is a continuing need to monitor albedo and roughness in order to identify possible trends and changes in surface energy balance.

Acknowledgements

This work was supported by a NASA grant entitled "Improving Arctic Energy Budgets by Combining New EOS-Era Products from Multiple Sensors". MISR data were provided courtesy of the NASA Langley Atmospheric Science Data Center. Dr. William Krabill of the NASA Wallops Flight Facility, Wallops Island, Virginia, graciously provided Lidar data from the Airborne Topographic Mapper. Dr. Ted Scambos of the National Snow and Ice Data Center, Boulder, Colorado provided the Greenland ice sheet digital elevation data. We greatly appreciate the helpful comments of the two anonymous reviewers.

References

Abdalati, W., & Steffen, K. (2001). Greenland ice sheet melt extent: 1979–1999. *Journal of Geophysical Research*, *106*(D24), 33983−33988.

Ambach, W. (1963). Untersuchungen zum Energieumsatz in der Ablationszone des grnlndischen Inlandeises (Camp IV-EGIG, 69°40′05″N, 49°37′58″W). *Meddelelser om Gronland*, *174*(4), 311.

Bader, H. (1961). The Greenland ice sheet. CRREL monogr. I-B2.

Benson, C. S. (1962). Stratigraphic studies in the snow and firn of the Greenland ice sheet. *U.S. Army cold regions research and engineering laboratory (CRREL) research report no. 70.* 120 pp.

Bindschadler, R. J., Dowdeswell, D., Hall, J. -G., & Winther (2001). Glaciological applications with Landsat-7 imagery: Early assessments. *Remote Sensing of Environment*, *78*, 163−179.

Braithwaite, R. J., & Olesen, E. B. (1993). Seasonal variation of ice ablation at the margin of the Greenland ice sheet and its sensitivity to climate change, Qamanarssup sermia, West Greenland. *Journal Glaciology*, *39*(132), 267−274.

Choudhury, B. J. (1981). Radiative properties of snow for clear sky solar radiation. *Cold Regions Science and Technol*, *4*, 103−120.

Colbeck, S. C. (1979). Grain clusters in wet snow. *Journal of Colloid and Interface Science*, *72*, 371−384.

Colbeck, S. C. (1982). An overview of seasonal snow metamorphism. *Reviews of Geophysical and Space Physics*, *20*, 45−61.

Colbeck, S. C. (1983). Theory of metamorphism of dry snow. *Journal of Geophysical Research*, *88*, 5475−5482.

Comiso, J. C. (2002). A rapidly declining perennial sea ice cover in the Arctic. *Geophysical Research Letters*, *29*. doi:10.1029/2002GL015650

Diner, D. J., Beckert, J. C., Bothwell, G. W., & Rodriguez, J. I. (2002). Performance of the MISR instrument during its first 20 months in orbit. *IEEE Transactions on Geoscience Remote Sensing*, *40*(7), 1449−1466.

Dozier, J., Schneider, S. R., & McGinnis Jr, D. F. (1981). Effect of grain size and snowpack water equivalence on visible and near-infrared satellite observations of snow. *Water Resources Research*, *17*, 1213−1221.

Duda, R. O., & Hart, P. E. (1973). Pattern classification and scene analysis. New York: Wiley. 482 pp.

Echelmeyer, K., Harrison, W. D., Clarke, T. S., & Benson, C. (1992). Surficial glaciology of Jakobshavns Isbrae, West Greenland: Part II. Ablation, accumulation and temperature. *Journal Glaciology*, *38*(128), 169−181.

Engeset, R. V., Kohler, J., Melvold, K., & Lundén, B. (2002). Change detection and monitoring of glacier mass balance and facies using ERS SAR winter images over Svalbard. *International Journal Remote Sensing*, *23*, 2023−2050.

Fahnestock, M., Bindschadler, R., Kwok, R., & Jezek, K. (1993). Greenland ice sheet surface properties and ice dynamics from ERS-1 SAR imagery. *Science*, *262*(5139), 1530−1534.

Forster, R. R., Isacks, B. L., & Das, S. B. (1996). Spaceborne imaging radar (SIR-C/X-SAR) reveals near-surface properties of the south Patagonian Icefield. *Journal of Geophysical Research*, *101*, 23169−23180.

Greuell, W., & de Ruyter de Wildt, M. (1999). Anisotropic reflection by melting glacier ice: Measurements and parameterizations in Landsat TM bands 2 and 4. *Remote Sensing of Environment*, *70*, 265−277.

Greuell, W., & Knap, W. H. (2000). Remote sensing of the albedo and detection of the slush line on the Greenland ice sheet. *Journal Geophysical Research*, *105*(D12), 15,567−15,576.

Hall, D. K., Ormsby, J. P., Bindschadler, R. A., & Siddalingaiah, H. (1987). Characterization of snow and ice reflectance zones on glaciers using Landsat Thematic Mapper data. *Annals of Glaciology*, *9*, 1−5.

Hall, D. K., Williams Jr, R. S., & Sigurdsson, O. (1995). Glaciological observations of Brúarjokull, Iceland, using synthetic aperture radar and thematic mapper satellite data. *Annals of Glaciology*, *21*, 271−276.

Hapke, B. (1993). Theory of reflectance and emittance spectroscopy Cambridge: Cambridge University Press. 455 pp.

Herzfeld, U. C., Mayer, H., Feller, W., & Mimler, M. (1999). Glacier roughness surveys of Jakobshavn Isbræ drainage basin, west Greenland, and morphological characterization. *Zeitschrift für Gletscherkunde und Glazialgeologie*, *35*, 117−146.

Hyvärinen, T., & Lammasniemi, J. (1987). Infrared measurements of free-water content and grain size of snow. *Optical Engineering*, *26*, 342−348.

IPCC. (2001). Climate change 2001: The scientific basis. In J. T. Houghton, Y. Ding, D. J. Griggs, M. Noguer, P. J. van der Linden, X. Dai, K. Maskell, & C. A. Johnson (Eds.), *Contribution of working group 1 to the third assessment report of the intergovernmental panel on climate change.* Cambridge: Cambridge University Press. 881 pp.

Joughin, I., Abdalati, W., & Fahnestock, M. (2004). Large fluctuations in speed on Greenland's Jakobshavn Isbrae glacier. *Nature*, *432*, 608−610. doi:10.1038/nature03130

Knap, W. H., & Oerlemans, J. (1996). The surface albedo of the Greenland ice sheet: Satellite-derived and in situ measurements in the Søndre Strømfjord area during the 1991 melt season. *Journal of Glaciology*, *42*, 364−374.

Knap, W. H., Reijmer, C. H., & Oerlmans, J. (1999). Narrowband to broadband conversion of Landsat TM glacier albedos. *International Journal Remote Sensing*, *20*, 2091−2110.

König, M., Wadham, J., Winther, J. -G., Kohler, J., & Nuttal, A. -M. (2002). Detection of superimposed ice on the glaciers Kongsvegen and midre Love'nbreen, Svalbard, using SAR satellite imagery. *Annals of Glaciology*, *34*, 335−342.

König, M., Winther, J. -G., & Isaksson, E. (2001). Measuring snow and glacier properties from satellite. *Reviews of Geophysics*, *39*, 1−27.

Krabill, W., Abdalati, W., Frederick, E., Manizade, S., Martin, C., Sonntag, J., et al. (2000). Greenland ice sheet: High-elevation balance and peripheral thinning. *Science*, *289*, 428−430.

Krabill, W., Frederick, E., Manizade, S., Martin, C., Sonntag, J., Swift, R., et al. (1999). Rapid thinning of parts of the southern Greenland ice sheet. *Science*, *283*, 1522−1524.

Long, D. L., & Drinkwater, M. R. (1994). Greenland observed at high resolution by the Seasat-A scatterometer. *Journal of Glaciology*, *40*, 213−220.

Marshall, G. J., Rees, W. G., & Dowdeswell, J. A. (1995). The discrimination of glacier facies using multi-temporal ERS-1 SAR data. In J. Askne (Ed.), *Sensors and environmental applications of remote sensing* (pp. 263–269). Brookfield, VT: A.A. Balkema.

Mock, S. J. (1967). Accumulation patterns on the Greenland ice sheet. *CRREL Research Report*, 233.

Mote, T. L., & Anderson, M. R. (1995). Variations in snowpack melt on the Greenland ice sheet based on passive microwave measurements. *Journal of Glaciology*, *41*(137), 51−60.

Nolin, A. W., & Dozier, J. (1993). Estimating snow grain size using AVIRIS data. *Remote Sensing of Environment*, *44*, 231−238.

Nolin, A. W., & Dozier, J. (2000). A hyperspectral method for remotely sensing the grain size of snow. *Remote Sensing of Environment*, *74*, 207−216.

Nolin, A., & Stroeve, J. (1997). The changing albedo of the Greenland ice sheet: Implications for climate change. *Annals of Glaciology*, *25*, 51−57.

Nolin, A. W., Fetterer, F. M., & Scambos, T. A. (2002). Surface roughness characterizations of sea ice and ice sheets: Case studies with MISR data. *IEEE Transaction on Geoscience and Remote Sensing*, *40*(7), 1605−1615.

Østrem, G. (1975). ERTS data in glaciology, an effort to monitor glacier mass balance from satellite imagery. *Journal of Glaciology*, *15*, 403−415.

Paterson, W. S. B. (1994). *The Physics of Glaciers* (3rd ed.). Oxford, United Kingdom: Elsevier Science Ltd. 481 pp.

Paterson, W. S. B., & Reeh, N. (2001). Thinning of the ice sheet in northwest Greenland over the past forty years. *Nature*, *414*, 60−62.

Partington, K. C. (1998). Discrimination of glacier facies using multitemporal SAR data. *Journal of Glaciology*, *44*(146), 42−53.

Rignot, E., & Kanagaratnam, P. (2006). Changes in the velocity structure of the Greenland ice sheet. *Science*, *311*, 986−990.

Rott, H., & Matzler, C. (1987). Possibilities and limits of synthetic aperture radar for snow and glacier surveying. *Annals of Glaciology*, *9*, 195−199.

Serreze, M. C., Walsh, J. E., Chapin, F. S., Osterkamp, T., Dyurgerov, M. B., Romanovsky, V., et al. (2000). Observational evidence of recent change in the northern high-latitude environment. *Climate Change*, *46*, 159−207.

Steffen, K., Abdalati, W., & Stroeve, J. (1993). Climate sensitivity of the Greenland ice sheet using satellite AVHRR, SMMR, SSM/I and in situ data. *Meteorology and Atmospheric Physics*, *51*, 239−258.

Stroeve, J. C., & Nolin, A. W. (2002). New methods to infer snow albedo from the MISR instrument with applications to the Greenland ice sheet. *IEEE Transaction on Geoscience and Remote Sensing*, *40*(7), 1616−1625.

Stroeve, J., Nolin, A., & Steffen, K. (1997). Comparison of AVHRR-derived and in situ surface albedo over the Greenland ice sheet. *Remote Sensing of Environment*, *62*(3), 262−276.

Thomas, R. T. (2004). Force-perturbation analysis of recent thinning and acceleration of Jakobshavn Isbrae, Greenland. *Journal of Glaciology*, *50*, 57−66.

Thomas, R., Akins, T., Csatho, B., Fahnestock, M., Gogineni, P., Kim, C., et al. (2000). Mass balance of the Greenland ice sheet at high elevations. *Science*, *289*, 426−428.

Vaughn, D. G., & Doake, C. S. M. (1996). Recent atmospheric warming and retreat of ice shelves on the Antarctic peninsula. *Nature*, *379*, 328−330.

Vermote, E. F., Tanre, D., Deuze, J. L., Herman, M., & Morcrette, J. -J. (1997). Second simulation of the satellite signal in the solar spectrum, 6S: An overview. *IEEE Transaction on Geoscience and Remote Sensing*, *35*, 675−685.

Warren, S. G. (1982). The optical properties of snow. *Reviews of Geophysics and Space Physics*, *20*, 67−89.

Warren, S. G., & Wiscombe, W. J. (1980). A model for the spectral albedo of snow, II, snow containing atmospheric aerosols. *Journal of the Atmospheric Sciences*, *37*, 2734−2745.

Warren, S. G., Brandt, R. E., & O'Rawe Hinton, P. (1998). Effect of surface roughness on bi-directional reflectance of Antarctic snow. *Journal of Geophysical Research*, *103*, 25789−25807.

Wiscombe, W. J., & Warren, S. G. (1980). A model for the spectral albedo of snow, I, pure snow. *Journal of the Atmospheric Sciences*, *37*, 2712−2733.

Williams, R. S., Jr., Hall, D. K., & Benson, C. S. (1991). Analysis of glacier facies using satellite techniques. *Journal Glaciology*, *37*, 120−127.

Zwally, H. J., Abdalati, W., Herring, T., Larson, K., Saba, J., & Steffen, K. (2002). Surface melt-induced acceleration of Greenland ice-sheet flow. *Science*, *297*, 218−222.

Zwally, H. J., Giovinetto, M. B., Li, J., Cornejo, H. G., Beckley, M. A., Brenner, A. C., et al. (2005). Mass changes of the Greenland and Antarctic ice sheets and shelves and contributions to sea-level rise: 1992–2002. *Journal Glaciology*, *51*, 509−527.